

# Multi-scale simulation of plant stem reinforcement by brachysclereids: A case study in apple fruit peduncles



Melanie Horbens<sup>a,\*</sup>, Dominik Branke<sup>b</sup>, Roland Gärtner<sup>c</sup>, Axel Voigt<sup>d</sup>, Florian Stenger<sup>d</sup>, Christoph Neinhuis<sup>a</sup>

<sup>a</sup> Technische Universität Dresden, Institute for Botany, Zellescher Weg 20b, 01217 Dresden, Germany

<sup>b</sup> Technische Universität Dresden, Institute for Solid Mechanics, George-Bähr-Straße 3c, 01069 Dresden, Germany

<sup>c</sup> Technische Universität Dresden, Institute for Lightweight Engineering and Polymer Technology, Holbeinstr. 3, 01307 Dresden, Germany

<sup>d</sup> Technische Universität Dresden, Institute for Scientific Computing, Zellescher Weg 12-14, 01217 Dresden, Germany

## ARTICLE INFO

### Article history:

Received 7 April 2015

Received in revised form 25 July 2015

Accepted 6 August 2015

Available online 13 August 2015

### Keywords:

Cellular architecture  
Diffuse domain approach  
Fibres  
Finite element analysis  
Modelling  
Sclereids

## ABSTRACT

Scleireid formation in addition to or in gaps of fragmented fibre rings is common in dicotyledonous plant stems. Whether this sclereid formation is force-triggered remains open so far. In fruit peduncles of several *Malus* species as modified plant stems, for example, the persistent fibre ring is displaced to the centre by formation of cortex parenchyma during growth. Parenchyma cells subsequently differentiate into an additional layer of brachysclereids, previously interpreted as an adaptation to continuously rising fruit loads. The present study pursues a multi-scale numerical modelling approach, to verify the important effect for different cellular architectures in both sclerenchyma categories on the stiffness of these tissues and the entire peduncle. First, different material properties are simulated analogue to plant tissues on the basis of three cell types. A regular three-dimensional and a random Voronoi microstructure combined with various mechanical cell wall parameters are applied. Using homogenisation simulations based on HILL's principle, numerical calculations predict a lower effective homogenised tissue stiffness of isodiametric brachysclereids compared to those of fibres, confirming experimentally obtained data from *Malus* fruit peduncles. Furthermore, a curved peduncle model with a complex arrangement of different material layers is generated. Diverse material sets are tested under three representative loadings, using an adaptive diffuse domain approach (AMDiS). The model explains the function of sclereids as considerable contributors to the stiffness against bending and tensile deformations, as well as torsion, especially in consequence of superimposed load conditions in the case of a curved plant stem.

© 2015 Elsevier Inc. All rights reserved.

## 1. Introduction

The hierarchical organisation enables plants in a fascinating way to adjust mechanical properties of tissues in response to environmental cues, such as mechanical loading (Speck and Burgert, 2011; Niklas, 2009). These structural adaptations depend on a multifactorial dynamical system. Cellulose microfibril orientation on the cell wall level determines stiffness and strength of plant stems as well as compositional modifications (e.g.: Reiterer et al., 1999; Köhler and Spatz, 2002; Burgert et al., 2004; Gindl et al., 2004; Burgert and Fratzl, 2009). Cell shape, relative tissue density, and especially tissue arrangement are crucial factors on tissue level (e.g.: Niklas, 1992; Speck and Burgert, 2011).

The load bearing tissue of dicotyledonous plant stems is frequently located in the periphery, addressing constructional principles of a material efficient, bending-resistant design (Niklas, 1992; Rees, 2009). *Malus* fruit peduncles, however, are highly modified plant stems. Apart from a thin peripheral layer of lamellar colenchyma, the peduncles possess a centrally located sclerenchyma (Horbens et al., 2014). Furthermore, the xylem that usually contributes to the flexural rigidity of young branches is strongly reduced. Nevertheless, the peduncle has to resist increasing fruit weight (up to 1600-times), resulting in rising static and dynamic stresses e.g. under oscillating wind loads. In addition to tensile forces, fruit peduncles attached to the branches in various orientations are exposed to considerable bending moments. The sclerenchyma comprises a ring of fibres that becomes relatively displaced towards the centre, due to radially expanding and dividing cortical parenchyma cells during growth, especially in species with heavy fruits (see Fig. 7 in Horbens et al., 2014). Simultaneously, brachysclereids differentiate outside the fibre

\* Corresponding author.

E-mail addresses: [melanie.horbens@tu-dresden.de](mailto:melanie.horbens@tu-dresden.de) (M. Horbens), [dominik.branke@tu-dresden.de](mailto:dominik.branke@tu-dresden.de) (D. Branke), [roland.gaertner@tu-dresden.de](mailto:roland.gaertner@tu-dresden.de) (R. Gärtner), [axel.voigt@tu-dresden.de](mailto:axel.voigt@tu-dresden.de) (A. Voigt), [florian.stenger@tu-dresden.de](mailto:florian.stenger@tu-dresden.de) (F. Stenger), [christoph.neinhuis@tu-dresden.de](mailto:christoph.neinhuis@tu-dresden.de) (C. Neinhuis).

ring. Cell walls of such sclereids differ in thickness. Massive secondary walls were observed especially in the wild species *Malus sylvestris*, thin secondary cell walls in species supporting lower fruit weight e.g. *Malus fusca*. Based on a biomechanical study, different mechanical functions and experimentally determined Young's moduli of fibres and brachysclereids have been found (Horbens et al., 2014). Besides variations in cell wall composition of both tissues, mainly cell shape and arrangement are suggested as functional explanation.

The present study takes up the geometrical differences between the two sclerenchyma categories fibres and brachysclereids using a numerical modelling approach. The model tests the effect of cell geometry on the mechanical properties of an entire curved stem, which is difficult to verify experimentally with acceptable precision. Fibres usually are long cells with tapered overlapping ends forming dense bundles, which originate from meristematic cells (Evert, 2006). By contrast, brachysclereids develop mostly from belated sclerified parenchyma cells characterised by an isodiametric shape and maintained intercellular spaces between neighbouring cells (Evert, 2006). The development of sclereids in gaps of a fragmented sclerenchyma ring is common in dicotyledonous plant stems (Wilson et al., 1983; Busch et al., 2010); also the formation of scattered sclereids with various shapes among the parenchymatous ground tissue of fruit pericarps (Romanov et al., 2011), leaves (Heide-Jorgensen, 1990), or flowers (Zhang et al., 2010).

Mathematical modelling of cellular mechanics contributes to a better understanding of structure–function–relationships of complex organised plants (Bruce, 2003; Godin and Sinoquet, 2005). Models serve as complements in addition to experimentally obtained data, or if they are difficult to obtain (e.g.: Silva et al., 2006; Nelson et al., 2012; Schwager et al., 2013; Joffre et al., 2014; Wang et al., 2014). Since each model represents an idealised system, predicted parameters are often not fully transferable to the plant system, but useful to estimate trends. Up to now many different approaches are suggested for different levels of hierarchy, reviewed in Bruce (2003). Special focus is paid to the simulation of the micromechanics of thin-walled, hydrated cells analogous to fruit parenchyma. A mesh-free particle framework model considers the interior liquid phase and viscoelastic properties of cell walls including time-dependent behaviour and failure mechanisms (Liedekerke et al., 2010a,b). Experimentally determined deformations of onion epidermal cells under tension are numerically described in good agreement by modelling a fibre-reinforced hyperelastic material (Qian et al., 2010). Ghysels et al. (2009) used a multi-scale model based on a mass-spring approach combined with a discretised macroscopic domain in standard finite elements to simulate large elastic deformations of epidermal cells. The irregular distribution of plant cells in tissues can be simulated by random cellular microstructures using the vectorisation of digital images, an ellipse tessellation algorithm, or the Voronoi tessellation method (e.g.: Li et al., 2005; Mebatsion et al., 2009; Béakou and Ntenga, 2011; Pieczywek et al., 2011; Faisal et al., 2014). Several simulations focused on secondary cell walls of wood (reviewed in Hofstetter and Gamstedt, 2009) considering varying orientations of microfibrils and chemical compositions within a multi-layered system (e.g.: Persson, 2000; Hofstetter et al., 2005; Béakou and Ntenga, 2011; Joffre et al., 2014). Stiffness and/or hydroelastic properties of hierarchically structured wood have been predicted within the elastic range using homogenisation procedures (e.g.: Persson, 2000; Hofstetter et al., 2005; Joffre et al., 2014).

In the present study we pursue a multi-scale approach, combining numerical models for different levels of hierarchy: the cell, tissue, and organ level. (1) Based on anatomical features of *M. sylvestris*, three representative geometrical cell models are generated applying a regular three-dimensional and a random Voronoi microstructure. (2) Combining these cell microstructures with

various mechanical cell wall parameters known from literature, five different materials representing the peduncle tissues collenchyma, parenchyma, fibres, thin-walled, and thick-walled brachysclereids are simulated by linear elastic homogenisation procedures based on HILL's principle, performed using finite element analysis (FEA). Calculated homogenised effective material parameters are compared with experimentally obtained data of separate tissue layers of *Malus* fruit peduncles. (3) The simulated materials are arranged in individual layers within a curved cylindrical structure analogous to a fruit peduncle, considering changing cross-sectional areas of the specific tissues along the longitudinal axis. (4) Using an adaptive diffuse domain approach (AMD<sub>i</sub>S), an effective method to solve partial differential equations of elasticity within complex geometries (Vey and Voigt, 2007; Li et al., 2009), stress states under three representative load conditions (tensile, bending and torsion tests) are numerically calculated. The model of cell/tissue level provides the basis for a simulated peduncle and is used to verify the postulated smaller Young's modulus of brachysclereids compared to fibres caused by different cell geometries. The model of organ level tests different material sets (model A–D) (i) to explain the reinforcing function and importance of the sclereid layer at this position, and (ii) to verify the effect of the cell geometry, cell wall thickness, and composition within this layer on the stiffness of the entire curved plant stem under different loadings. We assume the case that expanding and dividing cortical parenchyma cells remain unchanged during growth, the differentiation of thin-walled brachysclereids, and the formation of an additional fibre layer for comparison.

## 2. Material, methods, and model description

### 2.1. Plant material and experimental data

Matured fruits of the wild apples *M. sylvestris* and *M. fusca* are collected in the fruit gene bank of the Julius Kühn-Institute, Institute for Breeding Research on Horticultural and Fruit Crops, Dresden-Pillnitz, Germany. Anatomical features of the peduncle tissues parenchyma, brachysclereids, and fibres are quantified by light microscopy and image analyses of transverse sections. For more details see Horbens et al. (2014). Additionally, cell details have been examined by scanning electron microscopy (SEM) 'Supra 40VP' (Carl Zeiss MicroImaging GmbH, Oberkochen, Germany) at 5 kV acceleration voltages, after critical point drying and sputter-coating with gold palladium. To determine mechanical properties of separate tissue layers, at least 20 matured peduncles are successively bent in three-point bending tests (Zwick/Roell BZ 2.5/TS1S universal testing machine, Ulm, Germany) before and after the removal of individual tissue layers. The rigidity and Young's modulus of the removed layers are calculated, respectively, applying the Voigt model, which assumes a multi-layered composite girder. Methodical details are described in Horbens et al. (2014). These data serve for comparison and validation with numerical calculated values of the tissue-model.

### 2.2. Numerical model of different cell types

Based on anatomical specifics, numerical models of three cell geometries (cell level) are generated and developed in the finite element software ABAQUS (Dassault Systèmes Simulia GmbH, Aachen, Germany). The data set is presented in Table 1. Type I are spherical, thin-walled cells as repeated units, representing polyhedral, living parenchyma cells (Fig. 1a and d). This type is also used to simulate thin-walled brachysclereids. The contact surfaces of those spheres slightly merge into each other, resulting in a regular microstructure that forms a hexagonal package with a cell wall area proportion of about 16%. Gaps between spheres are treated as voids equipped with 'no medium' in conformity with air-filled intercellular spaces between parenchyma cells. The

**Table 1**  
Overview about anatomical specifics of different tissues determined in mature fruit peduncles of *M. sylvestris* and the chosen parameters of the corresponding simulated cell model.

Parameter	Cell-type I – parenchyma		Cell-type II – brachysclereids		Cell-type III – fibres	
	Model	<i>M. sylvestris</i>	Model	<i>M. sylvestris</i>	Model	<i>M. sylvestris</i>
Cell shape	Spherical	Polyhedral, isodiametric	Spherical	Polyhedral, isodiametric	Polyhedral, fibrous	Polyhedral, prosenchymatic
Intercellular conditions	Voids, no medium	Interc. spaces, air-filled	Voids, no medium	Interc. spaces, air-filled	Without voids	Without interc. spaces
Cell length ( $\mu\text{m}$ )					Endless	$430 \pm 63$
Cell diameter ( $\mu\text{m}$ )	31.0	$31.4 \pm 7.8$	39.4	$39.3 \pm 11.8$	10–16	$13.4 \pm 2.9$
Cell wall thickness ( $\mu\text{m}$ )	1.8	$1.9 \pm 0.4$	13.5	$14.6 \pm 3.2$	3–8	$5.8 \pm 1.4$
Cell lumen diameter ( $\mu\text{m}$ )	27.4	$27.6 \pm 5.2$	12.4	$9.2 \pm 5.7$	3.5	$1.8 \pm 0.6$
Cell fluid	Water*	Water	Water*	Water	Water*	Water
Relative cell wall area proportion (%)	16	$14.7 \pm 0.8$	70	$88.9 \pm 1.2$	93	$94.1 \pm 3.2$

Interc., intercellular.

\* The fluid inclusion was defined by a bulk modulus  $K = 2080$  MPa and an assumed ratio between the bulk and shear modulus  $G$  of 1/1000.

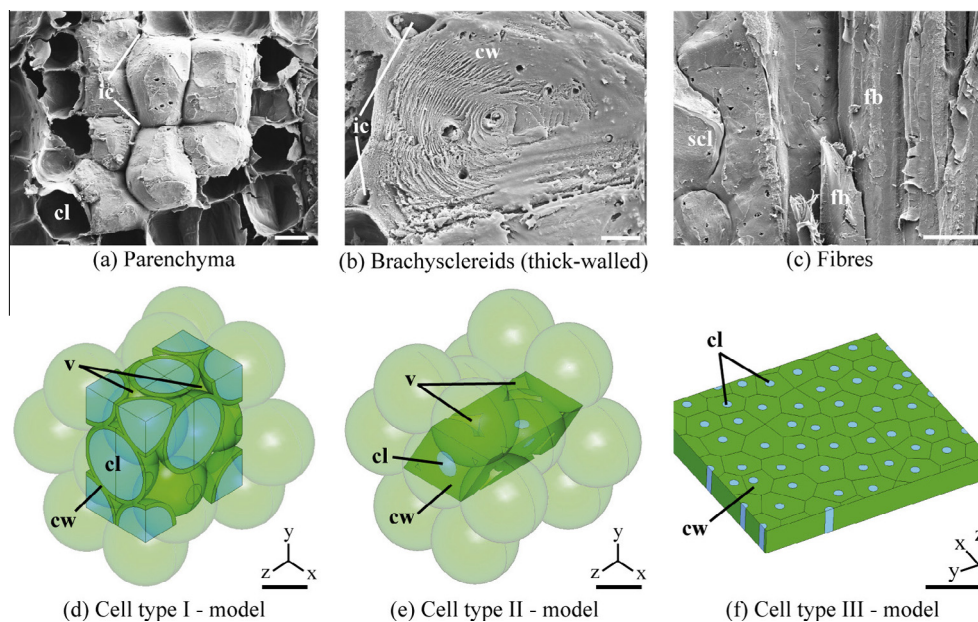


**Fig. 1.** (a–c) Scanning electron micrographs of the plant tissues parenchyma, brachysclereids (thick-walled), and fibres in fruit peduncles of *M. sylvestris*, and (d–f) the correspondingly simulated cell models. *Abbreviations:* cl, cell lumen; cw, cell wall; fb, fibres; ic, intercellular spaces; scl, brachysclereids; v, voids. Scale bars: (b) = 5  $\mu\text{m}$ ; (a, c–f) = 20  $\mu\text{m}$ .

protoplasm inside of parenchyma cells contains a large (80–90% of the cell volume), water-filled vacuole with ions whose inner hydrostatic cell turgor pressure (0.1–1 MPa) accounts for a large amount of the tissue stiffness (Niklas, 1992). According to in situ conditions, simulated cells are filled with a nearly incompressible aqueous medium. Type II are thick-walled brachysclereids as repeated units representing spherical cells arranged in a hexagonal package with a cell wall area proportion of about 70% (Fig. 1b and e). This type provides also the basis to simulate a simplified lamellar collenchyma.

Type III represents plant fibres with polyhedral cross-sections and an aspect ratio of about 32 modelled as endless cells (Fig. 1c and f). A two-dimensional cellular honeycomb-structure with an irregular cell shape and wall thickness is simulated using the Voronoi tessellation technique according to Li et al. (2005) and Faisal et al. (2014). The growth of circles with randomly distributed, hexagonally arranged nucleation points is simulated applying the same linear rate using an irregularity-parameter  $\alpha$  of 0.145. The tool has been developed in MATLAB (MathWorks, Ismaning, Germany). The Voronoi-pattern is extruded in normal direction to obtain a three-dimensional structure. Originating from

the nucleation points, a constant, circular interior water reservoir is assumed, resulting in a relative cell wall area proportion of about 93% without voids.

### 2.3. Numerical model of plant tissues

Five representative materials (tissue level) are generated to simulate individual peduncle tissues, as follows: (i) Type I provides the basis for the simulated parenchyma and thin-walled brachysclereids. (ii) Thick-walled brachysclereids and lamellar collenchyma are modelled applying type II. (iii) Type III is used for fibres. A single-layered epidermis of natural peduncles has been considered equal to collenchyma; the reduced xylem and the phloem analogous to parenchyma. Primary cell walls (parenchyma, collenchyma) are simulated using a Young's modulus  $E$  of 550 MPa and Poisson ratio  $\nu$  of 0.45, according to estimated cell wall moduli of 500–600 MPa given in Gibson (2012). A Young's modulus  $E$  of 8 GPa is chosen for lignified secondary cell walls (sclereids, fibres). The solid cell wall modulus of such cells may vary over three orders of magnitude from 0.1 to 45 GPa in lignified vascular bundles of palms (Gibson, 2012; Rüggeberg et al., 2008, 2009), or

from 5 to 30 GPa in tracheids of spruce (Burgert et al., 2005; Keunecke et al., 2008).

To calculate the engineering constants of each material (effective Young's modulus  $E^*$ , shear modulus  $G^*$ , and Poisson ratio  $\nu^*$ ), a linear elastic homogenisation procedure according to Hill (1963, 1972) is carried out using the finite element software ABAQUS (Dassault Systèmes Simulia GmbH, Aachen, Germany). The procedure is based on the equivalence of the stored stress power in the representative volume element (RVE) at the microscopic scale and the corresponding homogeneous region at the macroscopic scale. Imposing periodic boundary conditions to the RVE, the homogenised material properties are obtained by analysing the local stress fields after applying macroscopic strain states by means of local displacement fields.

The following assumptions are applied in the present model: (i) All computed results pertain only within the framework of small displacement gradients. The assumed linear elastic behaviour is permissible, considering that elastic properties dominate the viscous material behaviour in mature apple fruit peduncles (Horbens et al., 2014). (ii) The predicted effective material properties are based on varying isotropic parameters of the cell wall. This assumption is sustainable using the cell-types I and II, because the effect of microfibril orientation within cell walls should be strongly diminished by spherical cell geometries and the resulting averaging over various spatial orientations of cell walls. Two-dimensional imperfect honeycomb structures (basis for type III) can be regarded as isotropic (Li et al., 2005). Helically reinforced fibre cell walls, however, exhibit a strong anisotropy, distinctly pronounced in longitudinal direction. The influence of microfibril orientation, that result in orthotropic characteristics applying an analytical model based on a three-dimensional framework (Joffre et al., 2014), has not been considered in the cell-type III model, but will be discussed in detail.

## 2.4. Numerical model of a curved fruit peduncle using an adaptive diffuse domain approach

### 2.4.1. Geometry

Analogous to tissue arrangement in fruit peduncles of *M. sylvestris*, a representative peduncle model (organ level) comprising five different layers is prepared (Fig. 2a). Furthermore, the varying tissue distribution at three distinct parts is considered:

(1) the base connected to the branch, (2) the centre, and (3) the part connected to the fruits (Fig. 2e). Three constructed representative cross-sections are interconnected along a path within a curved cylinder (radius  $R$  of 32.5 mm). The respective material is assigned to each layer, where different materials are only selected for the third layer providing the basis for the peduncle models A–D (Fig. 2a–d). Model A with thick-walled brachysclereids represents the real tissue combination in fruit peduncles of *M. sylvestris*. Model B tests the case that cortical parenchyma cells remain unchanged during growth. Model C assumes the differentiation of thin-walled brachysclereids and model D of an additional fibre layer.

### 2.4.2. Diffuse domain approach

Deformations and the resulting stress states within a curved peduncle are numerically calculated using the computed engineering constants of simulated tissues (cf. chap. 2.3) (1) under three representative load conditions (tensile, bending, and torsion), and (2) with varying material sets (model A–D). A diffuse domain approach is used, introduced in Li et al. (2009) in a general mathematical setting. Instead of an explicit meshing of structures and explicit description of the equations and boundary conditions in a given domain, the geometry is only implicitly described (Fig. 2f) by a phase field function taking the values 1 inside the domain and 0 outside with a smooth transition, and the equations to solve are extended to a larger simpler domain by multiplying the equations with the phase field function. For methodical details see Appendix A.

### 2.4.3. Numerical calculations of loading tests

The front surface of the peduncle end is (1) inclined by  $1^\circ$  relative around the  $x$ -axis at bending tests, (2) pulled by 0.01 mm perpendicular to the cross-section at virtual tension tests, and (3) the ends twisted by  $1^\circ$  relative to centre of the face (along the  $y$ -axis) in torsion tests, while the other end is fixed (Fig. 3).

### 2.4.4. Transformation of stress states

Simulated stress states are transformed to a polar coordinate system adapted to the curved peduncle geometry, defining a radial direction  $r$  and a circumferential direction  $\vartheta$ . For details see Appendix B.

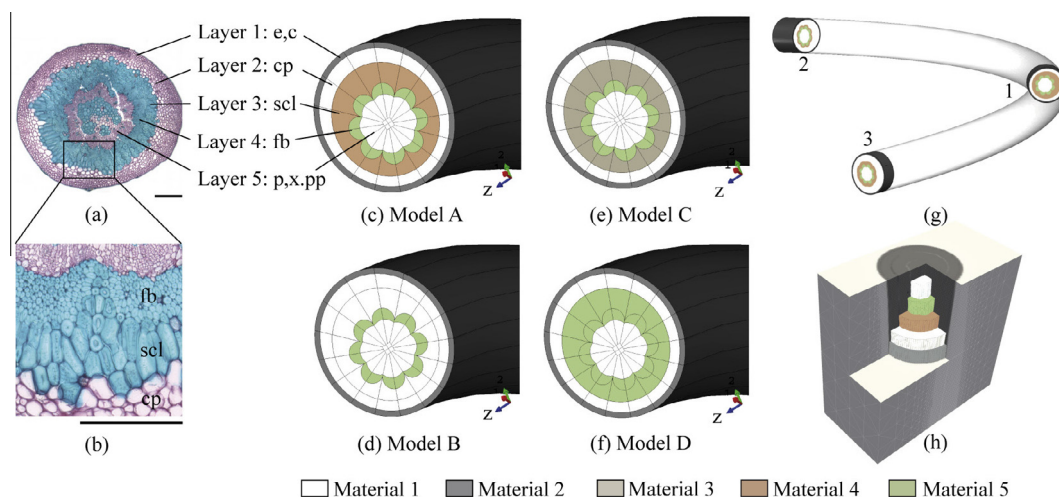


**Fig. 2.** (a–b) Representative transverse sections of fruit peduncles of *M. sylvestris* with details. (c–f) Peduncle models A–D based on five tissue layers. Model A represents the real tissue combination, the models B–D assume various material sets within layer three for comparison. The corresponding material properties are given in Table 3. (g) Curved peduncle model with three varying cross-sections along the longitudinal axis, representing tissue proportions at the centre (1), the connections to the branch (2), and to fruits (3). (h) Peduncle segment embedded in a regular cuboidal domain with an implicit volumetric mesh. Abbreviations: c, collenchyma; cp, cortical parenchyma; e, epidermis; fb, fibres; p, phloem; pp, pith parenchyma; scl, brachysclereids; x, xylem. Scale bars = 250  $\mu$ m.

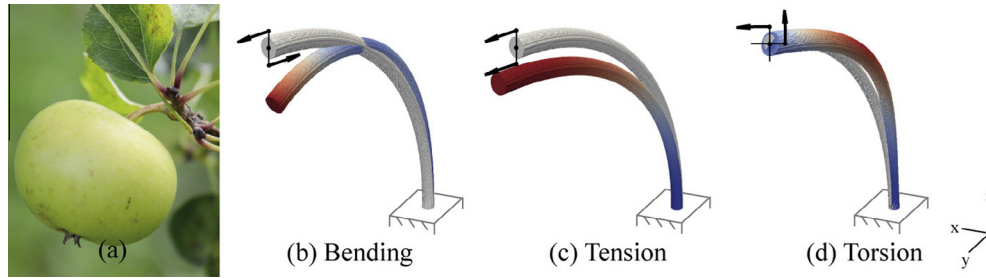


**Fig. 3.** (a) Fruit peduncle of *M. sylvestris* and (b–d) simulated bending, tensile, and torsion tests on the curved peduncle model. Arrows represent the direction of deformations applied at the front surface of the free peduncle end.

## 2.5. Data analyses

To quantify differences in simulated stress states between different peduncle models, the enclosed area of stress distribution plots at the position of layer 3 is determined as auxiliary quantity using an integration tool based on the trapezoidal rule (Software OriginPro, OriginLab Corporation, Northampton, USA).

## 3. Results

### 3.1. Experimentally obtained data from *Malus* fruit peduncles with isolated tissue layers

Experimentally obtained data, combined with the Voigt model obtained Young's moduli of individual peduncle layers of *M.*

**Table 2**

Experimental data obtained from three-point bending tests of fruit peduncles with isolated tissue layers.

Plant tissues within the peduncle layer	Young's modulus (MPa)	
	<i>M. sylvestris</i>	<i>M. fusca</i>
e, c, cp	155.7 ± 68.6	
e, c, cp, scl (thin-walled)		581.7 ± 137.2
scl (thick-walled)	2021.1 ± 554.3	
fb	6526.8 ± 1483.3	4071.4 ± 991.6

c, collenchyma; cp, cortical parenchyma; e, epidermis; scl, brachysclereids; fb, fibres.

**Table 3**

Calculated homogenised effective mechanical parameters of five materials to simulate different tissues obtained by the finite element analysis (FEA), and the assignment of these materials to the corresponding layer of the peduncle models in Fig. 2.

	Material 1	Material 2	Material 3	Material 4	Material 5
<i>Initial geometry and cell wall parameters:</i>					
Geometry	Cell-type I	Cell-type II	Cell-type I	Cell-type II	Cell-type III
Young's modulus, $E$ (MPa)	550	550	8000	8000	8000
Poisson ratio, $\nu$	0.45	0.45	0.45	0.45	0.45
<i>Calculated homogenised effective material parameters:</i>					
Young's moduli (MPa)					
$E_x^*$	46.4	398.4	654.9	5766.9	6998.4
$E_y^*$	46.5	398.4	656.6	5766.9	6995.2
$E_z^*$	45.1	395.5	637.3	5725.5	7511.7
Shear moduli (MPa)					
$G_x^*$	19.6	144.7	281.9	2105.2	2440.1
$G_y^*$	19.5	144.7	281.7	2105.0	2441.5
$G_z^*$	18.2	142.6	261.8	2073.3	2413.7
Poisson ratios					
$\nu_{yx}^*/\nu_{zx}^*$	0.278/0.306	0.397/0.403	0.252/0.280	0.391/0.397	0.447/0.451
$\nu_{xy}^*/\nu_{zy}^*$	0.277/0.314	0.397/0.406	0.251/0.287	0.391/0.400	0.447/0.420
$\nu_{xz}^*/\nu_{yz}^*$	0.315/0.314	0.406/0.406	0.288/0.287	0.400/0.400	0.421/0.420
<i>Basis of modelling for:</i>					
Plant tissues	Parenchyma	Collenchyma	Thin-walled brachysclereids	Thick-walled brachysclereids	Fibres
Peduncle layers	Layer 2, 3, 5	Layer 1	Layer 3	Layer 3	Layer 3, 4

*sylvestris* and *M. fusca* (differentiate thick- or thin-walled sclereids, respectively) are presented in Table 2. The respective outer layer of peduncles contained several tissues. Hence, the Young's modulus must be considered as an effective value of different tissues. The calculated Young's modulus of the fibre layer is based on pure cross-sectional areas of fibres.

### 3.2. Simulation of plant tissues based on different cell models

The numerically calculated homogenised engineering constants of each simulated material are presented in Table 3. As expected, the three-dimensional, regular spherical cell geometry results in approximately isotropic effective material properties of materials 1–4. By contrast, the simulated fibres (material 5) exhibit transverse isotropic characteristics pointing at one preferred direction, resulting in an about 517 MPa higher effective Young's modulus along the longitudinal axis ( $z$ -coordinate). The plane normal to the fibre axis is isotropic.

The increase in tissue density by 54% from material 1 to material 2, simulating the thickening of primary walls in spherical cells, results in about 8.7-fold higher effective tissue stiffness. Increasing the Young's modulus of cell walls from 550 to 8000 MPa in spherical cells, which implies a virtual lignification, results in an about 14 times higher tissue stiffness. The simulated thickening of secondary cell walls of material 3 increases the effective tissue stiffness of material 4 about 125 times (related to material 1). An additional geometrical modification of material 4 into simulated

endless fibres results in a 156 times higher effective Young’s modulus of the material 5 compared to material 1 or in 1.3 times higher values compared to material 4. Similar ratios described for Young’s moduli are observed for the effective shear moduli. In accordance with a microscopic model of parenchyma and collenchyma tissue, represented in Faisal et al. (2014), the differences between the Poisson ratios are rather small.

3.3. Simulation of a curved peduncle with different material sets loaded under three representative load conditions

In numerically calculated loading tests the predicted reaction forces/moments at the clamp and load application are used to verify differences in stiffness among the peduncle models A–D. Magnitudes of the respective forces/moments are normalised by values of the model B, representing the most compliant tissue combination. Simulated stress states within the central parts of peduncles models serve additionally as a measure for the stiffness (high stress magnitudes denote a high stiffness). However, these stresses can only be interpreted as average, representative values not providing conclusions about failure. Stress states are represented in distribution plots for each model and a given sectional plane, as well as in coloured plots across the section.

The applied bending increasing the peduncle curvature provokes reaction moments along the x-axis and an axial force at the load application ( $F_{yl}$ ) or radial force at the clamp ( $F_{yc}$ ) (Fig. 4c and d). The highest absolute values, which point to the strongest resistance against flexural deformations, shows the peduncle model D

characterised by an additional fibre layer. The model A with thick-walled sclereids exhibits about 20% smaller reaction forces and moments. As expected, the lowest resistance against flexural deformations is assigned to the model B followed by model C.

Considering the stress distribution plots focussed on the third peduncle layer, an equal tendency is observed in circumferential and radial stresses at the given sectional plane of 22.5° (Fig. 4a and b). While the respective difference in graphs between model A and D, or B and C is small but clearly noticeable, the material combinations in model A and D provoke significantly higher stresses indicating a greater peduncle stiffness. Based on ratios of the enclosed area segment of the stress curves at the position of layer 3 (Fig. 4a and b, marked in grey), the following factors should be used as auxiliary quantity, to compare differences among the peduncle models. The material combination of model A results in about 7.6-fold higher circumferential and radial stresses compared with model C, whereas model D causes about 1.2-fold higher stresses compared with those in model A. Differences in stress curves at the interface between the third and fourth peduncle layer arise from overlaps of the corresponding diffuse phase fields. Circumferential stresses  $\sigma_\theta$  are the dominant component exceeding about three times the radial stresses  $\sigma_r$ . By contrast, acting shear stresses  $\sigma_{r\theta}$  at maximum reach 5–7% of circumferential stresses. The maximum amounts of circumferential and radial stresses are located at the tensile (convex) and compression (concave) side within the fibre and sclereid layer of the model A, whereas these stresses are zero at the neutral fibre (Figs. 4a1,b1 and 5).

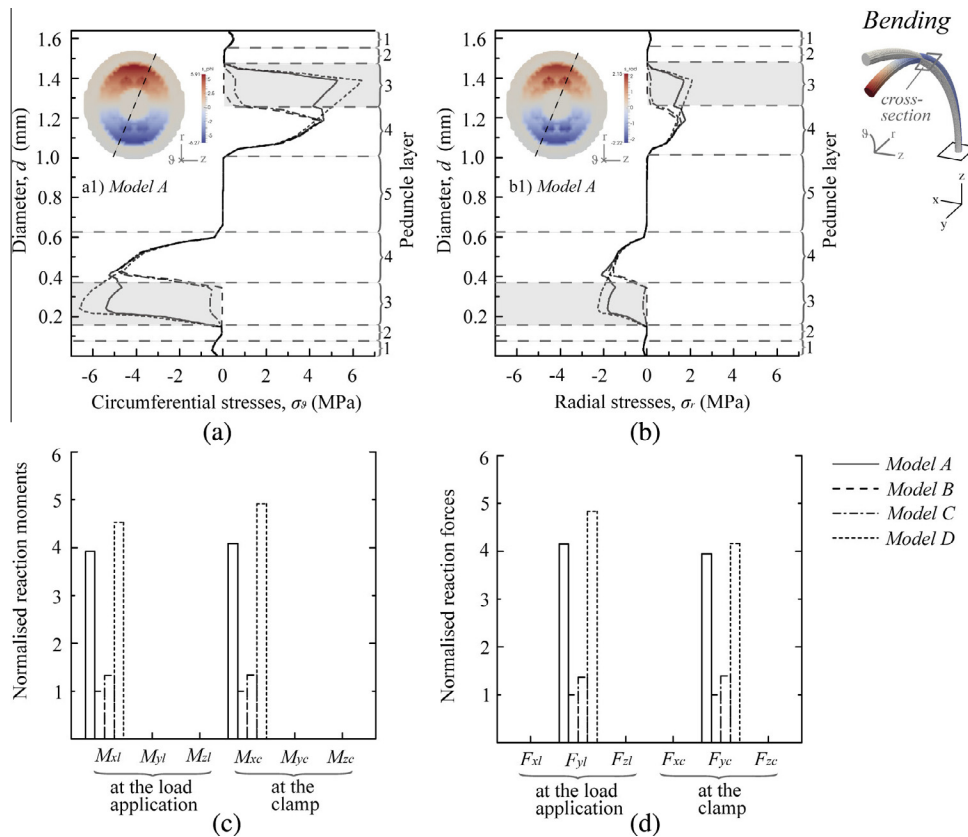
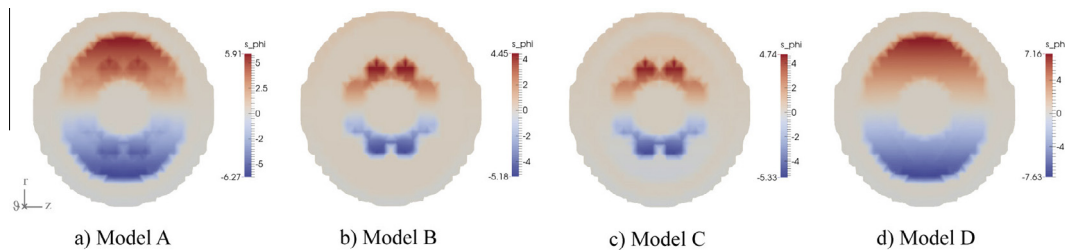


Fig. 4. Simulated bending tests performed on a curved peduncle model with different material sets (Model A–D). Distribution plots of (a) circumferential stresses  $\sigma_\theta$  and (b) radial stresses  $\sigma_r$  for each model across the central section at a given sectional plane of 22.5° (black dotted line), and (a1 and b1) coloured plots for the peduncle model A across the total section. The polar coordinate system (grey) is applied at the cross-section. Positive stress values define tensile, negative values compressive stresses (please note the varying scale). (c) Determined normalised reaction moments and (d) forces at the load application and clamp, respectively, related to the Cartesian coordinate system (black).



**Fig. 5.** Circumferential stresses  $\sigma_3$  in simulated bending tests represented in coloured distribution plots across the total middle section for different material sets (model A–D). Positive stress values define tensile, negative values compressive stresses (please note the varying scale).

The simulated stretching in direction of the  $y$ -axis evokes comparable ratios in reaction forces/moments between the individual models (Fig. 6a and b) as described under bending. Accordingly, the highest stiffness against tensile loading is found in the model D followed by the model A. The stress states within the considered cross-sections (Fig. 6a1 and b1) show the same trend, attributed to high proportions of an acting bending moment due to stretching of a curved structure. However, the curvature of the peduncle is decreased under the present load conditions. Consequently, stresses at the convex side possess a compressive character; those of the concave side are tensile stresses. The considered differences in area proportions of the stress curves within the third peduncle layer at the given sectional plane expose similar factors compared with those under bending.

In simulated torsion tests, the applied torsional moment along the  $y$ -axis provokes an additional bending moment along the  $z$ -axis, resulting in only small torsional reaction moments at the clamp ( $M_{yc}$ ). Ratios of reaction forces/moments among the individual models are comparable to those determined in bending and tension tests. Because the front surface can elude in  $y$ -direction, also a transverse force component ( $F_{xt}$ ) is induced upon loading. Under the present load case, the shear stress  $\sigma_{rz}$  is the dominant component (Fig. 6d). The magnitudes exceed circumferential stresses  $\sigma_3$  (Fig. 6c) by 10–14% in model B and C; but in the stiffer material compositions of the models A and D by 30–40%. The shear stress component  $\sigma_{rz}$  reaches equally high values in model A and D. When looking at the area proportions of the stress curves within the peduncle layer 3 at the given sectional plane of 67.5°, it is noticeable that the increase in shear stresses from model C to A was higher (up to 10-fold) compared with those under bending and stretching, while the rise from model A to model D comprises a comparable factor of 1.2. Resulting from the obviously dominant bending moment, the coloured stress distribution plots show also a neutral axis, and perpendicular to that plane the stress maxima/minima at the periphery (Fig. 6c1 and d1). While the highest magnitudes of circumferential stresses in model A are recognisable in layer 3 and 4, those of shear stresses are found in the periphery of layer 3 only.

#### 4. Discussion

The present multi-scale numerical modelling approach clearly demonstrates the different effects for cellular architectures in both sclerenchyma categories at the tissue level. Furthermore, the considerable contribution of the sclereid layer on the stiffness of the entire curved structure under three representative load conditions is explained.

##### 4.1. Validity of the used cell and tissue models

As expected, the calculated effective Young's modulus (399 MPa) of the material 1 exceeds experimentally obtained

values of 4–80 MPa for collenchyma of plant stems (Niklas, 1992, 1993), or 80–350 MPa for fruit skins comprising cuticle and various epidermal cell layers (Bargel and Neinhuis, 2005), due to the oversimplification of only tangentially thickened and slightly elongated cells. The effective Young's moduli for the simulated parenchyma (46 MPa) are in agreement with known values of 1–14 MPa for fruit parenchyma (Vincent, 1989; Niklas, 1993; Gibson, 2012), and 0.4–1 GPa for cortical parenchyma in stems of *Arundo donax* L. (Rüggeberg et al., 2009). Furthermore, the calculated effective Young's moduli for thin-walled brachysclereids (650 MPa) correspond approximately to experimentally obtained data from bending tests of fruit peduncles of *M. fusca* (Table 2). However, the calculated effective Young's modulus for thick-walled brachysclereids (5.7 GPa) exceeds 2.5 times the values from mechanical experiments (2 GPa) (Table 2, see Fig. 5 in Horbens et al., 2014); data from the literature are not available. The effective Young's modulus of simulated fibres (7 GPa) again matches experimentally obtained data of fibres (Table 2), or the stiffness of sclerenchyma strips (8–11 GPa) obtained from micro-tensile tests (Rüggeberg et al., 2009). Consequently, the present models provide a reasonable basis to estimate trends.

##### 4.2. Influence of cell geometry and cell wall properties at the tissue level

The present study underlines the well-known relationship between stiffness of plant tissues and cell wall composition, especially the degree of lignification (e.g. Gindl et al., 2004; Rüggeberg et al., 2008). Mechanical testing of lignin extracted sclerenchyma strips of stems of *Aristolochia*, for example, revealed 1.7 times smaller Young's moduli (Köhler and Spatz, 2002). Hence, the increase in the initial Young's modulus of cell walls, which implies a virtual lignification, exhibits the second largest influence on the calculated effective tissue properties. A strong increase in the effective tissue stiffness results also from the simulated thickening of thin-walled towards to thick-walled lignified sclereids (material 3 to 4), whereas the same increase in tissue density by 54% assuming primary cell walls (material 1 to 2) has a smaller effect (Table 3). The density-specific relationship to the tissue stiffness is particularly known from wood, where both the Young's modulus and strength directly correlate with density (Kollmann, 1951; Gibson, 2012). Furthermore, a relationship between Young's modulus and breaking stress has been demonstrated for fruit parenchyma, collenchyma, tracheids, and sclerenchyma of plant stems, although significance was only evident for parenchyma and wood (Vincent, 1989; Niklas, 1993).

The performed numerical model of plant tissues confirms the postulated smaller Young's modulus of thick-walled brachysclereids compared to fibres. However, the increase in the effective tissue stiffness from thick-walled spherical cells towards long fibres is comparatively small (factor 1.3), but distinctly visible. The present model primarily emphasises the impact of the higher

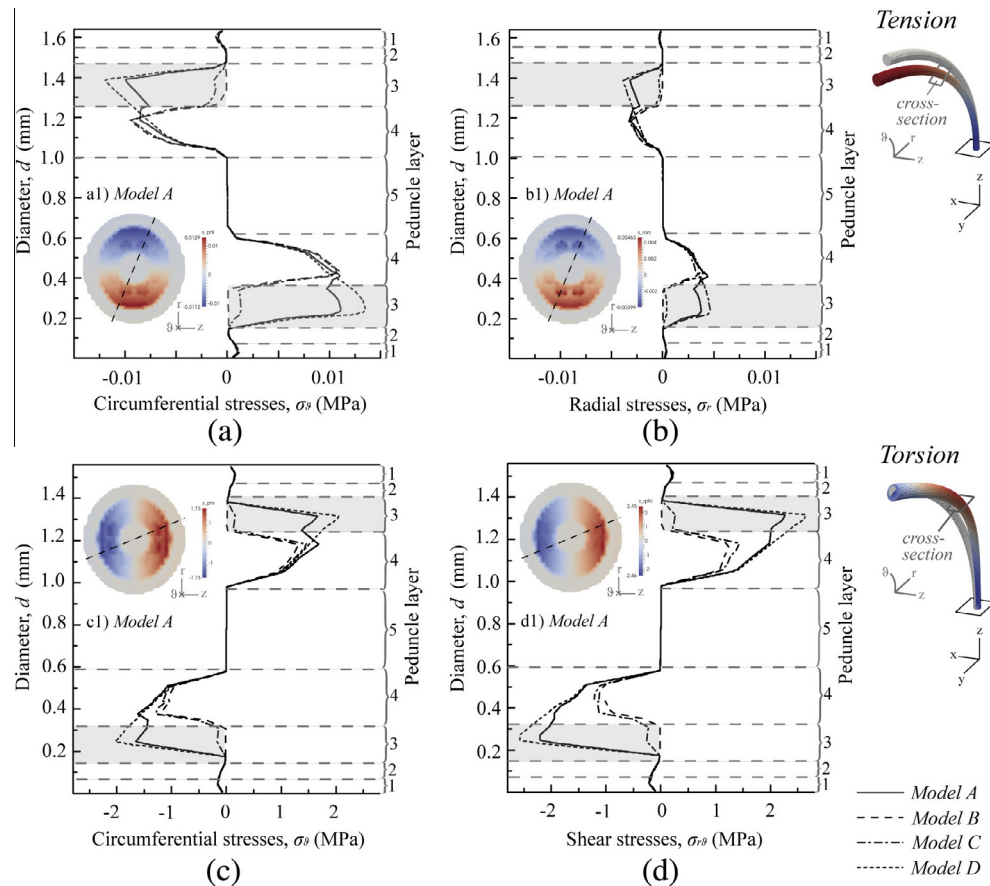


**Fig. 6.** (a and b) Simulated tensile and (c and d) torsion tests performed on a curved peduncle model with different material sets (model A–D). Distribution plots of (a and c) circumferential stresses  $\sigma_{\theta}$ , (b) radial stresses  $\sigma_r$ , and (d) shear stresses  $\sigma_{r\theta}$  for each model across the central section at a given sectional plane of 22.5° or 67.5° (black dotted line), and (a1–d1) coloured plots for the peduncle model A across the total section. The polar coordinate system (grey) is applied at the cross-section. Positive stress values define tensile, negative values compressive stresses (please note the varying scale).

relative density of fibre tissues (23 %) compared with thick-walled brachysclereids, due to lacking intercellular spaces between fibre cells. Even though the preferred direction in longitudinal axis of the virtual fibre tissue with transverse isotropic characteristics is taken into consideration, the significant impact of the microfibril orientation is not included. Multi-lamellar secondary cell walls are reinforced by cellulose fibrils with varying inclinations (e.g. 2–10° in flax and hemp fibres, or 5–20° in the S2 layer of wood tracheids). Small microfibril angles with respect to the longitudinal cell axis cause a high stiffness of secondary cell walls, resulting in only minor deformations prior to fracture (Reiterer et al., 1999; Köhler and Spatz, 2002; Burgert and Fratzl, 2009). This fact explains the higher difference (factor 3) in Young's moduli of thick-walled sclereids and fibres, experimentally obtained from fruit peduncles with isolated tissues (Table 2, see Fig. 5 in Horbens et al., 2014). Consequently, it may be expected that these differences in the effective elastic properties are more distinct along the longitudinal axis considering of the helically reinforced cell walls of fibres in the cell/tissue model.

#### 4.3. Function of brachysclereids in simulated curved peduncles under three representative load conditions

Apart from few other functions, such as light-guidance by foliar sclereids in evergreen sclerophylls (Karabourniotis, 1998), or facilitated water conduction to the epidermis by osteosclereids in some xeromorphic leaves (Heide-Jorgensen, 1990), the function of

sclereids commonly agreed on are: (1) sclereids in combination with fibres result in mechanical strengthening and play a protective role (Eschrich, 1995; Evert, 2006). Frequently, only the term “sclerenchyma” is used without any further differentiation, probably because the root of the term (*skleros*, meaning “hard”) already implies the function (Evert, 2006). (2) Brachysclereids absorb compressive stresses, fibres tension stresses in plants. Both statements are certainly not wrong, but they should be specified and substantiated by data, as explained below. Comparing the performed peduncle models A–D, we can explain the importance and reinforcing function of thick-walled brachysclereids at this position in curved peduncles.

The increase in the effective tissue stiffness from material 1 to 5 is reflected in the successive strengthening of the entire peduncle. The assumed differentiation of fibres, represented by model D, causes the highest stress magnitudes and reaction forces/moments (Figs. 4–6). Consequently, fibres are the most important reinforcing tissue under all representative load conditions. However, due to a lacking cambium in *Malus* fruit peduncles at this position, the differentiation of additionally fibres is not possible. The model A implies that the formation of thick-walled brachysclereid arising from expanding and dividing cortical parenchyma cells during growth results in a peduncle with an almost similar stiffness as compared to a peduncle with fibres only. Significantly lower magnitudes in stress distribution plots and reaction forces/moments determined for model C, which assumes the formation of thin-walled sclereids as observed in *Malus* species supporting lower

fruit weight, points to a strong reduced stiffness of the entire peduncle. The simulated case of unchanged remaining cortical parenchyma cells during growth (model B) demonstrates that only the fibre sheaths (layer 4) show stress magnitudes and contribute to the peduncle stiffness, which emphasise the importance of the additional brachysclereid formation. The proposed stiffening by brachysclereids and fibres mentioned above can be confirmed, (1) for small deformations, and (2) within the limits of stiffness differences due to cell shape and cell wall thickness. A comparable chemical composition of the cell walls is required as well, which has earlier been observed for fibres and brachysclereids in peduncles of *M. sylvestris*. Cellulose crystallinity index, however, is significantly lower in sclereids (Horbens et al., 2014).

The peripheral location of sclereids results in a fourfold higher axial second moment of area as that of the fibre ring, which can be considered as equal to the enlargement of the pre-existing fibre ring during growth. Stresses within thick-walled brachysclereids are of similar magnitudes as those in the fibre sheaths or exceed these values, apparent in stress distribution plots of model A (Fig. 4a and b). Hence, brachysclereid formation effectively stiffens the entire peduncle structure against bending deformations. Applying tension and torsion to a curved structure provokes also a bending moment, recognised from the stress-free neutral plane in cross-sections (Fig. 6a1–d1). Similar relations in predicted stress magnitudes and reaction forces/moments between peduncle model A and D suggest a comparable pertinent function of sclereids under tensile loading as a consequence of superimposed load conditions in curved structures. In experimental studies, however, the sclereid layer contributed only 35% to the axial rigidity, most probably explained by the exclusive application of tensile loads to rather straight samples (Horbens et al., 2014). Disproportionally higher shear stresses compared to circumferential stresses, provoked in simulated torsion tests of models A and D only, point out that sclereids and fibres in the position of the third layer effectively stiffen the peduncle structure also under torsion loads. The ‘filling’ of gaps in the partly constricted fibre ring results in a massive closed sclerenchyma ring, commonly contributed to a higher torsional stiffness (Rees, 2009). With respect to the second statement at the outset, the results of the present study prove the crucial role of the spatial arrangement of sclereids, since they contribute to the peduncle stiffness under all three load conditions, absorbing tensile, compressive, as well as shear stresses.

Fragmentation of peripheral fibre rings, caused by growth stresses or after injuries, is common in many dicotyledonous plant stems (Wilson et al., 1983). Brachysclereids differentiate from parenchyma cells adjacent to cracks, described as self-repair mechanism in liana stems (Busch et al., 2010). Whether this process is force-triggered remains open so far. Assuming small deformations, the plant stem will be comparably rigid after this ‘repair’, due to the relatively small difference in the effective Young’s moduli between thick-walled brachysclereids and fibres. However, the tensile strength, influenced by microstructural characteristics and predictable only if a statistical description of flaws is available (Bruce, 2003; Gibson, 2012), certainly cannot be re-established. A spherical cell shape results in reduced intercellular connections (Burgert et al., 2004). Numerous lignified middle lamellas as weakest link can induce flaws upon tensile loading. Interestingly, experiments applying local injury to *Ficus benjamina* showed that even the coagulation of latex significantly contributes to increased tensile strength (Bauer and Speck, 2012). By combining the spherical cell shape with the specific helicoidal cell wall architecture characterised by gradually alternating longitudinally and transversely oriented microfibrils (Roland et al., 1987; Reis and Vian, 2004), tissues of brachysclereids possess a rather isotropic material behaviour (Table 3). Precisely, that characteristic makes brachysclereids

suitable for stiffening a plant stem under different or superimposed load conditions. Furthermore, the clustering of brachysclereids directly adjacent to fibres may effectively prevent fibre buckling under compression.

## 5. Conclusions

The presented numerical model at the macroscopic scale elucidates the slightly lower effective, homogenised tissue stiffness of thick-walled brachysclereids compared to those of prosenchymatic fibres and confirms experimentally obtained data from *Malus* fruit peduncles. That effect is based primarily on the spherical/isodiametric cell shape of brachysclereids and maintained intercellular spaces. Simulation of a curved fruit peduncle model reflects the same trend. The model explains that additional formation of thick-walled brachysclereids considerably contributes to the stiffness under all three load conditions, absorbing tensile, compressive, as well as shear stresses, especially in consequence of superimposed load conditions at curved plant stems. The more isotropic material properties of brachysclereids seem to be effective in stiffening a plant stem under various loads. The previously used term ‘accessory’ cells for brachysclereids is justified concerning both, the limited effective tissue stiffness compared to fibres and the possibility of a fast differentiation of parenchyma cells into brachysclereids independent of an existing cambium in plants, which is essential for new fibre initials. The presented mechanism of a ‘self-reinforcing’ foam structure bears high biomimetic potential.

## Acknowledgements

This study was funded by the European Union (ERDF) and the Free State of Saxony (C2-13927/2379). The corresponding author thanks also the Graduate Academy of Technische Universität Dresden for financial support and two anonymous reviewers for suggestions that helped to improve the manuscript. We further acknowledge computing resources at ZIH at Technische Universität Dresden and JSC at Forschungszentrum Jülich.

## Appendix A. Diffuse domain approach

Boundary conditions of the phase field function are incorporated as penalty terms into the equation, with the penalty parameter related to the diffuse interface width of the smeared out boundary. By matched asymptotic analysis convergence to the original problem can be established if the diffuse interface width turns to zero. Numerical experiments even demonstrate second order convergence (Franz et al., 2012), which makes the approach computationally efficient. The approach has been successfully applied for various problems, e.g. elasticity and chemotaxis in complex biological structures (Aland et al., 2014; Landsberg et al., 2011). We here consider the same problem as in Aland et al. (2014), where the mathematical setting for linear elasticity and the different load conditions for tensile, bending, and torsion are described in detail. The only modifications are different material sets, a different geometry, and the use of five different phase field functions instead of one, to account for the five different layers with different elastic properties. We therefore do not write the equations here, but refer to Aland et al. (2014) for details. The resulting system is solved using the adaptive Finite Elements, with a fine grid resolution within the diffuse interface, such that approximately 5 grid points are within a cross-section of the interface. The resulting system of linear equation is solved by the iterative solver BiCGStab, implemented in the software AMDiS (Adaptive MultiDimensional Simulation) (Vey and Voigt,

2007; Witkowski et al., 2015), and solved in parallel on the high performance computer TAURUS.

## Appendix B. Transformation of stress states

The position of the clamp is fixed to  $\vartheta = 0^\circ$ , the load application to  $\vartheta = 90^\circ$ . To recalculate the stress states from the original Cartesian coordinates  $x$ ,  $y$ , and  $z$  in the adapted polar coordinate system, the following equations are used

$$\sigma_r = \frac{\sigma_{xx} + \sigma_{yy}}{2} + \frac{\sigma_{xx} - \sigma_{yy}}{2} \cos 2\vartheta + \sigma_{xy} \sin 2\vartheta, \quad (1)$$

$$\sigma_\vartheta = \frac{\sigma_{xx} + \sigma_{yy}}{2} - \frac{\sigma_{xx} - \sigma_{yy}}{2} \cos 2\vartheta - \sigma_{xy} \sin 2\vartheta, \quad (2)$$

$$\sigma_{r\vartheta} = -\frac{\sigma_{xx} - \sigma_{yy}}{2} \sin 2\vartheta + \sigma_{xy} \cos 2\vartheta, \quad (3)$$

To minimise disturbing effects due to boundary conditions at the clamp and load application, the stress states are compared between different peduncle models, only considering cross-sections of the middle peduncle position ( $\vartheta = 45^\circ$ ). The equations of stress transformation (1)–(3) are simplified to

$$\sigma_r = \frac{\sigma_{xx} + \sigma_{yy}}{2} + \sigma_{xy}, \quad (4)$$

$$\sigma_\vartheta = \frac{\sigma_{xx} + \sigma_{yy}}{2} - \sigma_{xy}, \quad (5)$$

$$\sigma_{r\vartheta} = -\frac{\sigma_{xx} - \sigma_{yy}}{2}. \quad (6)$$

## References

- Aland, S., Müller, R., Bobeth, M., Langheinrich, A.C., Voigt, A., 2014. Adaptive diffuse domain approach for calculating mechanically induced deformation of trabecular bone. *Comput. Methods Biomech. Biomed. Eng.* 17, 31–38.
- Bargel, H., Neinhuis, C., 2005. Tomato (*Lycopersicon esculentum* Mill.) fruit growth and ripening as related to the biomechanical properties of fruit skin and isolated cuticle. *J. Exp. Bot.* 56, 1049–1060.
- Bauer, G., Speck, T., 2012. Restoration of tensile strength in bark samples of *Ficus benjamina* due to coagulation of latex during fast self-healing of fissures. *Ann. Bot.* 109, 807–811.
- Béakou, A., Ntenga, R., 2011. Structure, morphology and mechanical properties of *Rhctophyllum camerunense* (RC) plant fiber. Part II: computational homogenization of the anisotropic elastic properties. *Comput. Mater. Sci.* 1550–1558.
- Bruce, D.M., 2003. Mathematical modelling of the cellular mechanics of plants. *Philos. Trans. R. Soc. A* 358, 1437–1444.
- Burgert, I., Fratzl, P., 2009. Plants control the properties and actuation of their organs through the orientation of cellulose fibrils in their cell walls. *Integr. Comp. Biol.* 49, 69–79.
- Burgert, I., Frühmann, K., Keckes, J., Fratzl, P., Stanzl-Tschegg, S., 2004. Structure–function relationships of four compression wood types: micromechanical properties at the tissue and fibre level. *Trees* 18, 480–485.
- Burgert, I., Eder, M., Frühmann, K., Keckes, J., Fratzl, P., Stanzl-Tschegg, S., 2005. Properties of chemically and mechanically isolated fibres of spruce (*Picea abies* [L.] Karst.). Part 3: mechanical characterisation. *Holzforchung* 59, 354–357.
- Busch, S., Seidel, R., Speck, O., Speck, T., 2010. Morphological aspects of self-repair of lesions caused by internal growth stresses in stems of *Aristolochia macrophylla* and *Aristolochia ringens*. *Proc. R. Soc. B* 277, 2113–2120.
- Eschrich, W., 1995. Funktionelle Pflanzenanatomie, 1st ed. Springer, Berlin.
- Evert, R.F., 2006. *Esau's Plant Anatomy*, 3rd ed. Wiley, Hoboken, New Jersey.
- Faisal, T.R., Hristozov, N., Western, T.L., Rey, A.D., Pasini, D., 2014. Computational study of the elastic properties of *Rheum rhabarbarum* tissues via surrogate models of tissue geometry. *J. Struct. Biol.* 185, 285–294.
- Franz, S., Gärtner, R., Roos, H.-G., Voigt, A., 2012. A note on the convergence analysis of a diffuse-domain approach. *Comput. Methods Appl. Math.* 12, 153–167.
- Ghysels, P., Samaey, G., Tijskens, E., Liedekerke, P.V., Ramon, H., Roose, D., 2009. Multi-scale simulation of plant tissue deformation using a model for individual cell mechanics. *Phys. Biol.* 6, 016009.
- Gibson, L.J., 2012. The hierarchical structure and mechanics of plant materials. *J. R. Soc. Interface* 9, 2749–2766.
- Gindl, W., Gupta, H.S., Schöberl, T., Lichtenegger, H.C., Fratzl, P., 2004. Mechanical properties of spruce wood cell walls by nanoindentation. *Appl. Phys. A* 79, 2069–2073.
- Godin, C., Sinoquet, H., 2005. Functional–structural plant modelling. *New Phytol.* 166, 705–708, Commentary.
- Heide-Jorgensen, H.S., 1990. Xeromorphic leaves of *Hakea suaveolens* R. Br. IV. Ontogeny, structure and function of the sclereids. *Aust. J. Bot.* 38, 25–43.
- Hill, R., 1963. Elastic properties of reinforced solids. Some theoretical principles. *J. Mech. Phys. Solids* 11, 357–372.
- Hill, R., 1972. On constitutive macro-variables for heterogeneous solids at finite strain. *Proc. R. Soc. Lond. A* 326, 131–147.
- Hofstetter, K., Hellmich, C., Eberhardsteiner, J., 2005. Development and experimental validation of a continuum micromechanics model for the elasticity of wood. *Eur. J. Mech. A-Solid* 24, 1030–1053.
- Hofstetter, K., Gamstedt, E.K., 2009. Hierarchical modelling of microstructural effects on mechanical properties of wood. A review. *Holzforchung* 63, 130–138.
- Horbens, M., Feldner, A., Höfer, M., Neinhuis, C., 2014. Ontogenetic tissue modification in *Malus* fruit peduncles: the role of sclereids. *Ann. Bot.* 113, 105–118.
- Joffre, T., Neagu, R.C., Bardage, S.L., Gamstedt, E.K., 2014. Modelling of the hygroelastic behaviour of normal and compression wood tracheids. *J. Struct. Biol.* 185, 89–98.
- Karabourniotis, G., 1998. Light-guiding function of foliar sclereids in the evergreen sclerophyll *Phillyrea latifolia*: a quantitative approach. *J. Exp. Bot.* 49, 739–746.
- Keunecke, D., Eder, M., Burgert, I., Niemez, P., 2008. Micromechanical properties of common yew (*Taxus baccata*) and Norway spruce (*Picea abies*) transition wood fibers subjected to longitudinal tension. *J. Wood Sci.* 54, 420–422.
- Köhler, L., Spatz, H.-C., 2002. Micromechanics of plant tissues beyond the linear-elastic range. *Planta* 215, 33–40.
- Kollmann, F., 1951. *Technologie des Holzes und der Holzwerkstoffe*, 2nd ed. Springer, Berlin.
- Landsberg, C., Stenger, F., Deutsch, A., Gelinsky, M., Rösen-Wolff, A., Voigt, A., 2011. Chemotaxis of mesenchymal stem cells within 3D biomimetic scaffolds—a modeling approach. *J. Biomech.* 44, 359–364.
- Li, K., Gao, X.-L., Subhash, G., 2005. Effects of cell shape and cell wall thickness variations on the elastic properties of two-dimensional cellular solids. *Int. J. Solids Struct.* 42, 1777–1795.
- Li, X., Lowengrub, J., Rätz, A., Voigt, A., 2009. Solving PDEs in complex geometries: A diffuse domain approach. *Commun. Math. Sci.* 7, 81–107.
- Liedekerke, P.V., Ghysels, P., Tijskens, E., Samaey, G., Smeets, B., Roose, D., Ramon, H., 2010a. A particle-based model to simulate the micromechanics of single-plant parenchyma cells and aggregates. *Phys. Biol.* 7, 026006.
- Liedekerke, P.V., Tijskens, E., Ramon, H., 2010b. Particle-based model to simulate the micromechanics of biological cells. *Phys. Rev.* 81, 061906.
- Mebatsion, H.K., Verboven, P., Endalew, A.M., Billen, J., Hoa, Q.T., Nicolaï, B.M., 2009. A novel method for 3-D microstructure modeling of pome fruit tissue using synchrotron radiation tomography images. *J. Food Eng.* 93, 141–148.
- Nelson, M.R., Band, L.R., Dyson, R.J., Lessinnes, T., Wells, D.M., Yang, C., Everitt, N.M., Jensen, O.E., Wilson, Z.A., 2012. A biomechanical model of anther opening reveals the roles of dehydration and secondary thickening. *New Phytol.* 196, 1030–1037.
- Niklas, K.J., 1992. *Plant Biomechanics: An Engineering Approach to Plant Form and Function*, 1st ed. University of Chicago Press, Chicago, IL.
- Niklas, K.J., 1993. Influence of tissue density-specific mechanical properties on the scaling of plant height. *Ann. Bot.* 72, 173–179.
- Niklas, K.J., 2009. Functional adaptation and phenotypic plasticity at the cellular and whole plant level. *J. Biosci.* 34, 613–620.
- Persson, K., 2000. *Micromechanical modelling of wood and fibre properties* (Doctoral thesis), University Lund.
- Piecznyk, P.M., Zdunek, A., Umeda, M., 2011. Study on parameterisation of plant tissue microstructure by confocal microscopy for finite elements modelling. *Comput. Electron. Agric.* 78, 98–105.
- Qian, M., Wells, D.M., Jones, A., Becker, A., 2010. Finite element modelling of cell wall properties for onion epidermis using a fibre-reinforced hyperelastic model. *J. Struct. Biol.* 172, 300–304.
- Rees, D.W.A., 2009. *Mechanics of optimal structural design: minimum weight structures*, 1st ed. Wiley, New York.
- Reis, D., Vian, B., 2004. Helicoidal pattern in secondary cell walls and possible role of xylans in their construction. *C. R. Biol.* 327, 785–790.
- Reiterer, A., Lichtenegger, H., Tschegg, S., Fratzl, P., 1999. Experimental evidence for a mechanical function of the cellulose microfibril angle in wood cell walls. *Philos. Mag. A* 79, 2173–2184.
- Roland, J.C., Reis, D., Vian, B., Satiat-Jeunemaitre, B., Mosiniak, M., 1987. Morphogenesis of plant cell walls at the supramolecular level: internal geometry and versatility of helicoidal expression. *Protoplasm* 140, 75–91.
- Romanov, M.S., Bobrov, A.V.F.C., Wijesundara, D.S.A., Romanova, E.S., 2011. Pericarp development and fruit structure in borassoid palms (*Arecaceae*–*Coryphoideae*–*Borasseae*). *Ann. Bot.* 108, 1489–1502.
- Rüggeberg, M., Speck, T., Burgert, I., 2008. Stiffness gradients in vascular bundles of the palm *Washingtonia robusta*. *Proc. R. Soc. B* 275, 2221–2229.
- Rüggeberg, M., Speck, T., Burgert, I., 2009. Structure–function relationships of different vascular bundle types in the stem of the Mexican fan palm (*Washingtonia robusta*). *New Phytol.* 182, 443–450.
- Schwager, H., Masselter, T., Speck, T., Neinhuis, C., 2013. Functional morphology and biomechanics of branch–stem junctions in columnar cacti. *Proc. R. Soc. B* 280, 20132244.
- Silva, E.C.N., Walters, M.C., Paulino, G.H., 2006. Modeling bamboo as a functionally graded material: lessons for the analysis of affordable materials. *J. Mater. Sci.* 41, 6991–7004.

- Speck, T., Burgert, I., 2011. Plant stems: functional design and mechanics. *Annu. Rev. Mater. Res.* 41, 169–193.
- Vey, S., Voigt, A., 2007. AMDiS: adaptive multidimensional simulations. *Comput. Vis. Sci.* 10, 57–67.
- Vincent, J.F.V., 1989. Relationship between density and stiffness of apple flesh. *J. Sci. Food Agric.* 47, 443–462.
- Wang, N., Liu, W., Huang, J., Mach, K., 2014. The structure-mechanical relationship of palm vascular tissue. *J. Mech. Behav. Biomed. Mater.* 36, 1–11.
- Wilson, J.W., Dircks, S.J., Grange, R.I., 1983. Regeneration of sclerenchyma in wounded dicotyledon stems. *Ann. Bot.* 52, 295–303.
- Witkowski, T., Ling, S., Praetorius, S., Voigt, A., 2015. Software concepts and numerical algorithms for a scalable adaptive parallel finite element method. *Adv. Comput. Math.* <http://dx.doi.org/10.1007/s10444-10015-19405-10444>.
- Zhang, W., Wang, X.-Q., Li, Z.-Y., 2010. The protective shell: sclereids and their mechanical function in corollas of some species of *Camellia* (Theaceae). *Plant Biol.* 13, 688–692.